



## Computational Effects of Winglet Tilted Within Range of $-45^\circ$ and $+45^\circ$ on the Up-Scale Wind Turbine Blade Using CFD

Patrick Irungu Muiruri<sup>1,2\*</sup>, Oboetswe Seraga Motsamai<sup>1</sup>

<sup>1</sup> Faculty of Engineering and Technology, Mechanical Engineering Department, University of Botswana (UB), Private Bag 0061, Gaborone, Botswana

<sup>2</sup> Materials and Manufacturing Engineering, Mechanical Engineering Department, Jomo Kenyatta University of Agriculture and Technology (JKUAT), School of Mechanical, P.O Box 62000-00200, Nairobi, Kenya

Corresponding Author Email: [pmuiruri@jkuat.ac.ke](mailto:pmuiruri@jkuat.ac.ke)

<https://doi.org/10.18280/mmep.070117>

**Received:** 12 November 2019

**Accepted:** 25 February 2020

### Keywords:

*aerodynamic-torque, axial force, bending-load, CFD-simulation, tangential force, winglet*

### ABSTRACT

The effects associated with the tilted blade tip section on power production and bending load are presented in this study. The blade tip's section of 0.045R size was inclined to the pressure and suction sides for cant angles within a range of  $-45^\circ$  to  $+45^\circ$ . National Renewable Energy Laboratory (NREL) 5MW wind turbine blade was used as a reference blade. The numerical computations were performed using the finite volume method through ANSYS Fluent version 19.1. First, the aerodynamic performance of different configurations was examined based on computation results of axial force, aerodynamic torque and bending load on flap-wise direction. The best performing blade configuration was selected for further investigations on pitch angle sensitivity for varying wind speed between rated wind speed and cut-out wind speed. A steady-state pressure based solver utilizing Semi-Implicit Method for Pressure Linked Equations (SIMPLE) algorithm was used to solve Reynolds Average Navier-Stoke (RANS) equations closed with  $k-\omega$  Shear Stress Transport (SST) turbulence model. All blades with winglets increase aerodynamic torque. The winglets inclined to the suction side result in a higher increase of aerodynamic torque than the corresponding winglets tilted to the pressure side. The winglet tilted by a cant angle of  $15^\circ$  produced the highest aerodynamic torque increment by about 10% as compared to other blades with winglets. A similar performance trend was observed for the blade with and without winglet when the pitch angle was varied according to the specified wind speed. The general conclusion was made that a winglet can be used to enhance power extraction without the necessity to increase the rotor diameter.

## 1. INTRODUCTION

Wind is a viable source of energy and can be utilized as an alternative source to fossil fuels. It is clean, abundant and widely distributed across the world [1]. A wind turbine is a machine that enables the conversion of kinetic energy harnessed from wind into electric power. Technological advancement to improve the designs of wind turbines to make wind energy competitive against other renewable energy sources are ongoing. One of the strategies employed by industries in order to increase harnessing of wind energy is to increase the rotor diameter. One hundred and sixty-three wind energy experts concluded that increasing the size of the wind turbine rotors would increase the annual wind power generation, and as a result decreases the costs of energy per kilowatts [2]. Large wind turbines can produce twice the amount of energy produced by a medium-sized wind turbine, which also cause the maintenance and operation costs to drop drastically [3]. Based on this, manufacturers and wind turbines industries are focusing on production of large wind turbines with big rotor diameter. However, the weight, transportation, installation and control of large wind turbines remain as a challenge for horizontal axis wind turbines, as

long as their rotor diameter continue to increase in size [4, 5].

A small load-carrying aerodynamic device known as winglet that is used to decrease the span-wise flow, diffuse and move the tip vortex away from the rotor plane by reducing the downwash resulting in induced drag is being tested for wind turbine application [6]. In the past, winglets were used on fixed-wing aircraft as a measure to reduce consumption of fuel by reducing the induced drag [7-9]. Application of winglet technology to wind turbine rotor blade could provide an alternative of increasing wind power generation without necessarily increasing the rotor diameter [10, 11]. For a blade without a winglet, the airflow at the blade-tip moves inwards on the suction surface and outwards on the pressure side, thereby generating vortices at the blade-tip edge and trailing edge of the blade. Application of winglet to the wind turbine can, therefore, not only improves the aerodynamic performance of the rotor but also reduces the noise emissions caused by the presence of vortices at blade-tip [12].

Guanna and Johansen [10] investigated maximum aerodynamic efficiency of wind turbine rotors with winglets using Free Wake Lifting Line (FWLL) method and Computational Fluid Dynamics (CFD) code EllipSys3D.

Their findings indicated that shorter downwind winglets  $>2\%$  resulted in close to the increased coefficient of power ( $C_p$ ) obtained by a radial extension of the wing. Gupta and Amano [11] investigated an inclined winglet to the pressure side for wind turbine with a rotor of 20 m radius using CFD method in ANSYS Fluent. The winglet's cant angle was inclined to  $90^\circ$  and  $45^\circ$ , and the winglet's height of  $2\%$  and  $4\%R$  where  $R$  is the radius of the rotor. The winglet's curvature remained constant at  $50\%$  of the rotor radius. The authors' findings revealed that winglets with cant angles of  $45^\circ$  resulted in higher increase in power production as compared to the winglet of the same height but inclined to pressure side by  $90^\circ$ . Increase in the winglet's height for a winglet of  $90^\circ$  from  $2\%$  to  $4\%R$  showed no significant increase in power production. Johansen and Sørensen [6] investigated four winglet's parameters namely winglet's height, curvature radius sweeps and twist for winglet inclined at  $90^\circ$  to the suction side of rotor blades. Computational results revealed that mechanical power and thrust increases with a decrease in curvature radius, while sweeping the winglet by  $30^\circ$  backwards has no effect on increasing mechanical power. Twisting the winglet resulted in little impact on mechanical power too.

Elfarra et al. [13] investigated aerodynamic effects of winglet inclined at cant angles of  $45^\circ$  and  $90^\circ$  with no twist angle and a twist angle of  $2^\circ$  such that four sets of configurations were established. The first and second sets had the winglets inclined to the pressure and suction sides while, the third and fourth sets had the winglets bent to the leading edge and trailing edge sides. Winglets pointing to the suction side resulted in better aerodynamic performance as compared to other configurations. Imamura et al. [14] investigated aerodynamic performance of the winglets on a two-bladed wind turbine rotor model. A winglet attached at the blade-tip and bent to the suction side was examined for different cant angles given as follow:  $10^\circ$ ,  $20^\circ$ ,  $40^\circ$  and  $80^\circ$ . Lawton and Crawford [15] used Implicit Free Wake Vortex Method (IFWVM) to investigate and optimize three winglets inclined at cant angles of  $90^\circ$ ,  $78.54^\circ$  and  $74.54^\circ$ .

Most of previous research on application of winglets to wind turbine blades investigates effects of winglets inclined at cant angle of either  $90^\circ$  or  $45^\circ$  to the pressure and suction sides. Results revealed that inclining winglet by  $90^\circ$  to the downstream direction for a winglet's height more than  $4\%R$  would cause rotor blade to strike tower due to blade-tip deflection, leading to production of less mechanical power as compared to winglets tilted at  $45^\circ$ . There is little literature published on winglets embedded on wind turbine blades investigating cant angles within a range of  $-45^\circ$  and  $45^\circ$ .

In this study, therefore, effects of blade-tip section equivalent to  $4.5\%$  of the rotor radius were tilted on both pressure and suction sides. Blades with winglets were developed without considering the winglet's curvature radius. All the blades with winglets had the same length as original blade without a winglet. This study was implemented in two phases. First, the study evaluated the best performing blade with a winglet based on comparison to the original straight blade in terms of tangential force, axial force (thrust), aerodynamic torque and bending moment on flap-wise direction. Second phase of this study examined the influence of pitching angles in terms of aerodynamic torque and bending moment production at hub based on the best performing blade, selected from the first phase of the study.

Pitching angle was varied in respect to operational offshore

wind speed of the National Renewable Energy Laboratory (NREL) 5MW which ranged from 11.4 to 25 m/s [16].

The next part of this paper is organized as follow: Section two (2) briefly describes benchmarking baseline wind turbine with emphasis on the design of the blade. Section three (3) presents design methodology of a blade with different winglet configurations. Computational Fluid Dynamic (CFD) methodology is presented in section four (4). Section five (5) presents results and discussion. Section six (6) draws conclusion of findings, and Section seven (7) provides insights into future work.

## 2. BASELINE WIND TURBINE

Offshore NREL 5 MW reference wind turbine [16] was taken as a benchmark for this study. This wind turbine is a conventional, upwind Horizontal Axis Wind Turbine (HAWT) with three rotor blades, which are rotated collectively using a pitch control system. The selected features of this wind turbine are listed in Table 1. The NREL 5 MW wind turbine baseline blade is shown in Figure 1.

**Table 1.** Selected features of NREL 5MW baseline Wind Turbine [16]

Features	Properties/Valus
Rating	5 MW
Rotor orientation, Configuration	Upwind, 3 Blades
Control	Variable speed, Collective Pitch
Drive train	High speed, Multiple stage gearbox
Rotor and Hub Diameter	126m, 3m
Hub Height	90m
Cut in, Rated, Cut out	3m/s, 11.4m/s 25m/s
Cut in, Rated, Rotor Speed	6.9 rpm, 12.1 rpm
Rated Tip Speed	80 m/s
Overhang, Shaft tilt, Precone	5m, $5^\circ$
Rotor Mass	110,000kg
Nacelle Mass	240,000kg
Tower Mass	347,460 kg
Coordinate location of overall CM (-0.2m, 0.0m, 64.0m)	

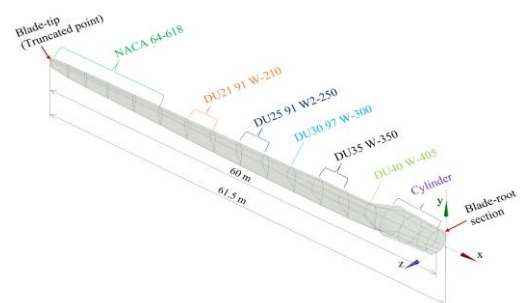


**Figure 1.** Baseline blade geometry modelled using ANSYS Design Modeller

## 3. DESIGN METHODOLOGY FOR BLADES WITH WINGLETS

The benchmarking blade was modified by creating a small

aerodynamic device known as winglet at the blade-tip without changing the sweep area of the rotor using Geometric-Modeler in ANSYS 19.1. The geometric parameters considered include a cant angle ( $\phi$ ), swept angle ( $\varphi$ ) and height (H) of the winglet, whereas other parameters such as toe angle and winglet curvature were not taken into account. A blade-tip section equivalent to 4.5%R was tilted to both pressure and suction sides at different cant angle, such that the winglet's height is less than overhanging distance between the tower and rotor of the reference NREL 5 MW wind turbine, which is equal to 5 m [16]. The cant angle ( $\phi$ ) was varied within the range of  $-45^\circ$  and  $+45^\circ$ , then swept back by a sweep-back angle of  $48^\circ$ , whereas a similar twist to the original blade was retained. The length of the corresponding winglet wetted section ( $L_w$ ) and the height of the winglet (H), were calculated as follow

Length of the winglet ( $L_w$ )

$$L_w = \frac{0.045 R}{\cos \phi} \quad (1)$$

Height of the winglet (H)

$$H = 0.045R \cdot \tan \phi \quad (2)$$

The geometric parameter matrix of the designed winglets is presented in Table 2. In Table 2, the blade with a winglet is designated as B-W, where “B” stands for the blade and “W” stands for the winglet. The digit designates the number of designed cases or design configuration. The sample of a blade designed with a winglet is shown in Figure 2.

**Table 2.** Design matrix of the winglets

Deflection side	cases	Cant angle	Height (H)	Length ( $L_w$ )
Pressure side	B-W1	-45	-2.730	3.861
	B-W2	-30	-1.576	3.152
	B-W3	-20	-0.994	2.923
	B-W4	-15	-0.732	2.826
	B-W5	-10	-0.481	2.772
Suction side	B-W6	10	0.481	2.772
	B-W7	15	0.732	2.826
	B-W8	20	0.994	2.923
	B-W9	30	1.576	3.152
	B-W10	45	2.730	3.861

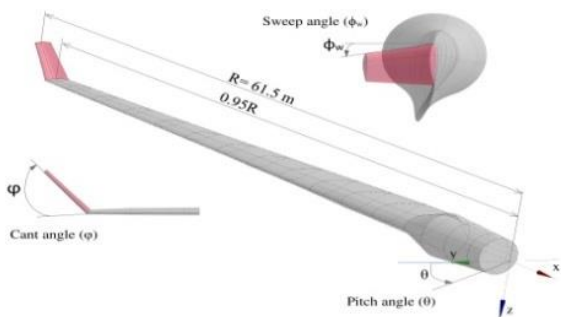


**Figure 2.** Blade with a winglet

## 4. COMPUTATIONAL FLUID DYNAMIC (CFD) SIMULATIONS

Only one of the three blades were simulated in this study. The other two blades were accounted for using the periodic boundary conditions because the three blades of the given wind turbine are fixed to the hub symmetrically at  $120^\circ$  apart. This strategy does not only drastically reduce the mesh elements required for simulation but also improves computational efficiency. All the other parts of wind turbines are outside the scope of this work.

### 4.1 Simulation domain

Figure 3 illustrates the simulation domain and blade set-up in the domain.

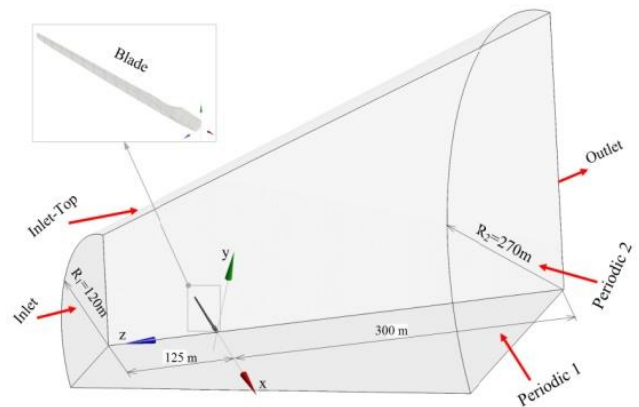


**Figure 3.** Simulation fluid domain

The simulation domain has a conical cylindrical shape. The inlet radius is 2.25 times less than outlet radius. The simulation domain presented in Figure 3 was adopted in this study. It is assumed that energy can only be extracted from a change in kinetic energy, hence velocity of the wind stream (the wind velocity behind the wind turbine) has to be less than the wind velocity in front of the wind turbine. That means an increase in the area, and the density change is considered insignificant [17]. The inlet boundary is positioned at 125m upstream, whereas the outlet boundary located at 300m downstream away from the position of the blade.

### 4.2 Meshing

The fluid computational domain was discretized into small-unstructured mesh cells. Near the blade surface, prismatic wedge cells were created by inserting fifteen inflation layers around the blade surface. The first thickness of inflation layers was set to  $3.2 \times 10^{-5} m$  in order to capture the boundary layer correctly such that the result of wall  $y^+$  is less than 5. Inflation layers were defined to grow with rate of 1.1. According to Ariff et al. [18], the necessitated dimensionless value of wall  $y^+$  should not exceed a range of between 30 to 300 for a fully turbulent region. The sphere influence meshes of 1m size were generated around the blade from centroid of the blade for a radius of 50m. The applied strategy eliminates the need of creating partitions in the fluid domain for purpose of refining the mesh around the blade surface. Small mesh cells reduce discretization errors during simulation.

Figure 4 shows the mesh independency; where

aerodynamic torque was plotted against number of mesh elements. The mesh elements increase with a decrease in the size of blade surface mesh starting from 0.15 to 0.03m. This mesh sensitivity study was adapted from previous work [19]. The blade face mesh of 0.05m was found adequate to model a blade without winglet at satisfactory computation speed as well as resulting in acceptable accuracy margin based on other published numerical results as indicated in the next section on validation of results. The mesh size of 0.05m was therefore adopted in the present study for blades with winglets.

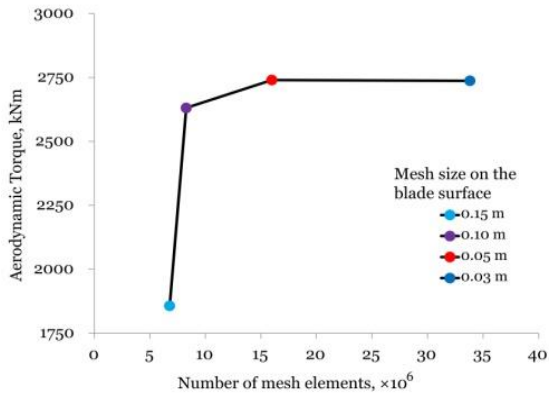


**Figure 4.** Plot of aerodynamic torque against total mesh elements for different blade surface mesh sizes

Figures 5 and 6 show mesh elements generated in the fluid domain with emphasis focusing on mesh near and around the blade surface.

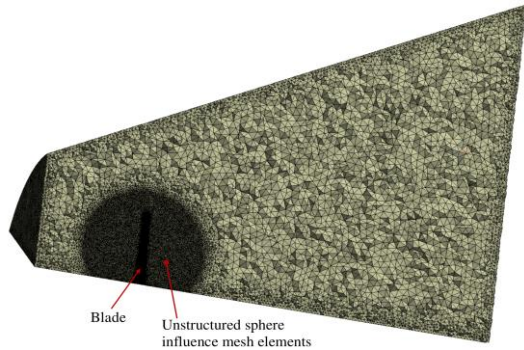


**Figure 5.** Sectioned fluid domain showing mesh elements with attention to the area around the blade surface

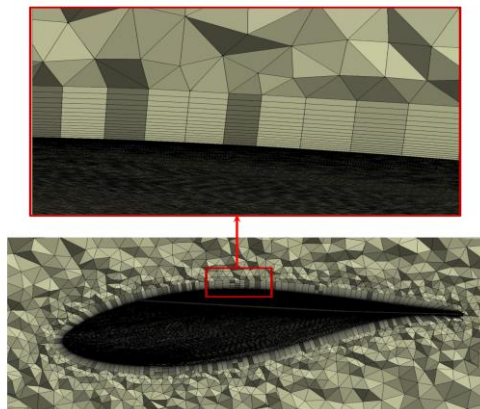


**Figure 6.** Zoomed mesh elements around the blade surface

The quality of mesh elements was determined using skewness and orthogonal criteria. It was found that skewness range within 0 and 0.98, while orthogonal quality range between 0.03 and 1.0. Small percentage of poor quality mesh elements was examined near the blade-tip section at the trailing edge. This was attributed to sharp edge of the blade trailing edge, even though NACA64-618 airfoil was truncated at 0.5% from trailing edge to reduce sharpness.

### 4.3 Boundary conditions

The boundary conditions for CFD simulation of the blades with different winglet sizes were defined as follow: at inlet, an average wind speed of 25m/s was specified, while at the outlet, zero-gauge pressure was defined. Periodic boundary conditions were imposed on two sides of the fluid domain to account for the other two blades. For flow velocity below 20 m/s, turbulent viscosity ratio and intensity were retained as default values in the ANSYS Fluent solver. That is, at both inlets and outlet boundaries, the turbulent viscosity ratio was specified as 10%, while turbulent intensity was set at 5%. For the fluid flow velocity above 20m/s, turbulent viscosity ratio and intensity were increased to 15% and 10% respectively, since turbulence was deemed to increase with an increase in flow velocity. The blade surface was defined as a wall with no-slip boundary condition. The single reference frame was set to rotate anticlockwise with an angular velocity equivalent to the rotational speed similar to that of the baseline wind turbine rotational speed, which is 12.1 rpm (refer to Table 1). To investigate the effects of a winglet with change in blade pitch angle for the best performing selected blade configuration, inflow velocities at inlet and inlet-top were changed within a range of 11.4 m/s and 25 m/s as indicated in Table 3 below.

**Table 3.** Pitch angle corresponding to wind

Items	Variables						
Wind speed (m/s)	11.4	13.0	15.0	18.0	20.0	23.0	25
Pitch Angle (°)	0.0	6.6	10.45	14.92	17.47	21.18	23.47

### 4.4 ANSYS fluent setting

In this study, the wind turbine was assumed to operate under subsonic flow regime, so the Mach number is less than 0.3. The tip-speed ratio ranges between 6.83 and 3.11 for wind speed within 11.4 m/s and 25 m/s, since the rotor radius is 61.5m. Fluid flow considered incompressible. Compressibility effects near the blade-tip edge were neglected.

Three-dimensional double precision and parallel scheme was used in all simulations. A similar simulation set-up used in our previous work [19], was adopted in this study. A steady pressure based solver under absolute velocity formulation was used to solve fluid flow governing equations using Semi-Implicit Method for Pressure Linked Equations (SIMPLE) algorithm. This algorithm decouples the momentum and continuity equations in a segregated manner. A second-order discretization scheme was used for pressure interpolation, while second-order upwind scheme was used for momentum, diffusion and conservative terms. Their

gradients were calculated using Least Squares Cell-Based method.

Residual values and thrust force were used to monitor convergence of given calculations per iteration. Residual criteria are widely used for monitoring the CFD calculations convergence. All residuals tolerances were set to drop below  $10^{-6}$ , slightly lower than the recommended value of at least  $10^{-4}$  [20]. A hybrid initialization method was applied to determine the initial variable values with reference to primary inlet boundary conditions. The calculations were performed iteratively up to a set of 8000 iterations. The question on whether the flow in domain was resolved, a continuity principle was used to check net mass flux flow between Inlet, Inlet-Top and outlet. The flow in present simulations were deemed well solved, since the net mass flux was computed to range between 0.002 kg/s and 0.004 kg/s.

The distribution of wall  $y^+$  values on the blade surface was found to adequately capture the boundary layer on the blade surface, since the maximum wall  $y^+$  value was found to be less than 5 as shown in Figure 7.

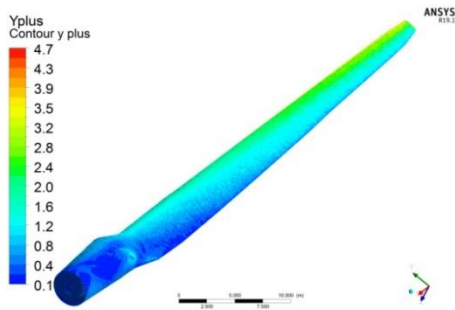


Figure 7. Distribution of dimensionless wall  $y^+$  value on the blade surface

#### 4.5 Validation of numerical simulation

Validation presented in this work was adopted from previous work [19]. It was performed for a blade without winglet following operating conditions: wind speed of 9 m/s, rotational speed of blade,  $\Omega = 10.3 \text{ rpm}$ , fluid viscosity,  $\mu = 1.82 \times 10^{-5} \text{ kg}\cdot\text{s}/\text{m}$  and fluid density,  $\rho = 1.225 \text{ kg}/\text{m}^3$ .

Comparison of computed results to results of other researchers [16, 21-24] is shown in Table 4.

Table 4. Comparison of computed aerodynamic torque to other numerical results of similar blade [19]

Model	Solver	Torque (kNm)
Jonkman et al. [16]	FAST	2500
Bazilevs et al. [21]	NURBS	2670
Siddiqui et al. [22]	OpenFoam	2650
Siddiqui et al. [23]	OpenFoam	2800
Zhao et al. [24]	OpenFoam	2682
$k-\omega$ SST	Fluent	2664
$k-\varepsilon$ RNG	Fluent	2740
$k-\varepsilon$ Realizable	Fluent	2768

Result of  $k-\omega$  SST was identified to be in close

agreement with other simulations as compared to results obtained for  $k-\varepsilon$  RNG and  $k-\varepsilon$  Realizable, hence it was selected for this study.

## 5. RESULTS AND DISCUSSION

The computational forces and moments of the blades with winglets were compared to results of a straight baseline blade. Figure 8, indicates the directions of forces and moments exerted at the hub of the rotor.

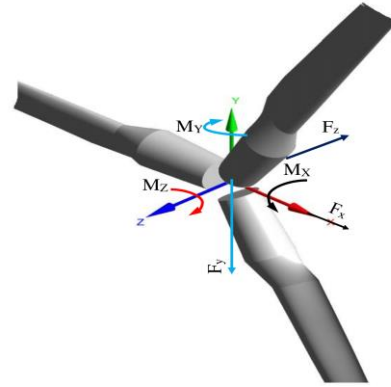


Figure 8. Direction of the forces and moments exerted at the hub of wind turbine rotor

### 5.1 Comparison of forces

Blades with different winglet configurations were simulated using similar operating conditions. The computational tangential and axial forces obtained for the blades with different winglet configurations were compared to simulation results of the straight baseline blade. For better comparison and visualization, results are presented in form of bar charts. Figures 9 and 10 show the comparative analysis of the tangential and axial forces for blades with different winglets respectively. The negative cant angles on the abscissa's axis represent winglets inclined to the pressure side, while the positive cant angles represent winglets tilted to the suction side. The red line cuts across the bar charts represent computational results of the straight baseline blade without a winglet.

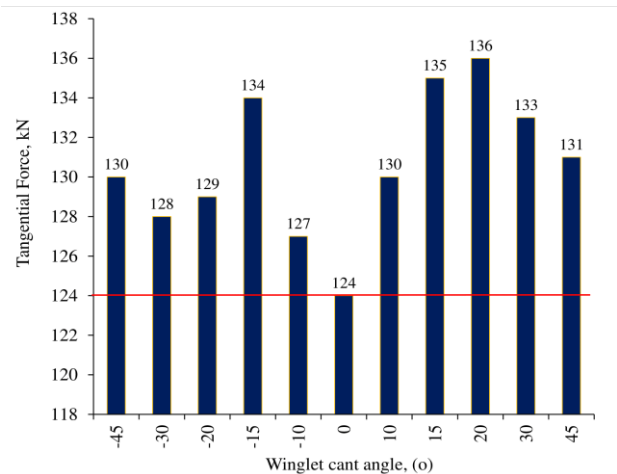


Figure 9. Comparison of tangential force of the blades with different winglet configurations



**Figure 10.** Comparison of axial force of the blades with different winglet configurations

From Figures 9 and 10, it is seen that the tangential and axial forces slightly vary from one blade configuration to the other. Blades with winglets pointing to the suction side resulted in the highest values of axial and tangential forces as compared to those with winglets pointing to the pressure side. It is not clear to the author why the blades with winglets pointing to the pressure side yield non-uniform trends on prediction of tangential and axial forces as compared to the corresponding winglets tilted to the suction side, despite using same operational conditions for all simulations. Authors of this paper, suggest that this could be influenced by curvature of blade profile towards the upstream affecting pressure distribution that is not in symmetry. The highest tangential force was obtained by the blade with a winglet of 20° cant angle, while the lowest tangential force results in the blade with winglet of -10° as shown in Figure 9. Comparison of axial forces showed similarity to those observed for tangential forces as displayed in Figure 10, where the maximum obtainable axial force was calculated for the blade with winglet of 20° cant angle and minimum force for the with winglet of -10° cant angle. Variation of cant angle and orientation of winglet to the suction side significantly influences forces (tangential and axial forces) induced at the blade as compared to the corresponding winglets pointing to the pressure side.

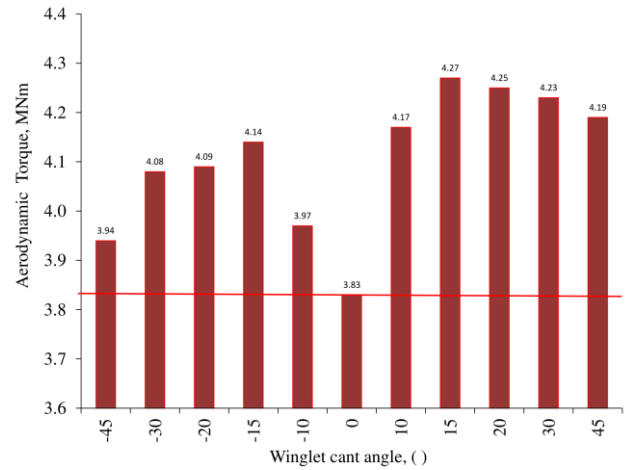
## 5.2 Comparison of moments

The moments due to Z-axis and Y-axis at the origin of the coordinate system are referred to as aerodynamic torque  $M_z$  and flap-wise bending load  $M_y$  respectively in this context. The computed aerodynamic torque and flap-wise bending load were compared to the results of the straight baseline blade as displayed in Figure 11 and 12 respectively.

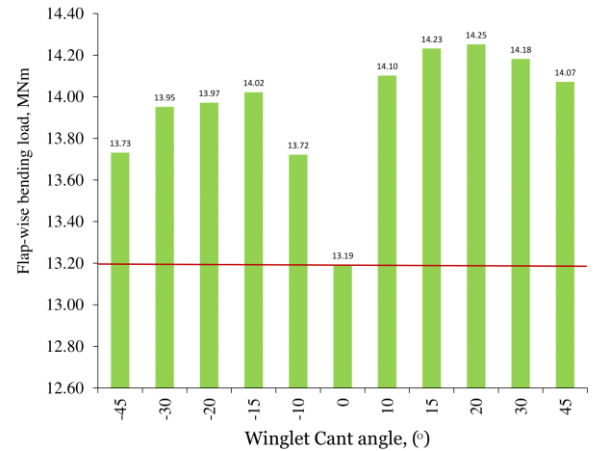
In Figure 11, blades with winglets pointing to the suction side generated more aerodynamic torque than their corresponding blades with winglets pointing to the pressure side. The same scenario is also observed for flap-wise bending load as shown in Figure 12. These loads are as result of air-load (pressure), which is distributed on the blade surface. The pressure coefficient distributed on the blade surface was computed using equation below

$$C_p = \frac{P - P_\infty}{0.5\rho(U_\infty^2 + (r\Omega)^2)} \quad (3)$$

where,  $C_p$  the coefficient of pressure,  $P$  is the static pressure,  $P_\infty$  is the pressure of moving air,  $\rho$  is the flow density,  $U_\infty$  is the flow velocity,  $r$  is the instantaneous radius of blade and  $\Omega$  is the rotational speed of the rotor.

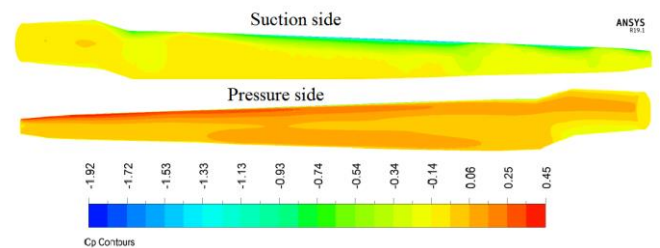


**Figure 11.** Comparison of aerodynamic torque of the blades with different winglet configurations



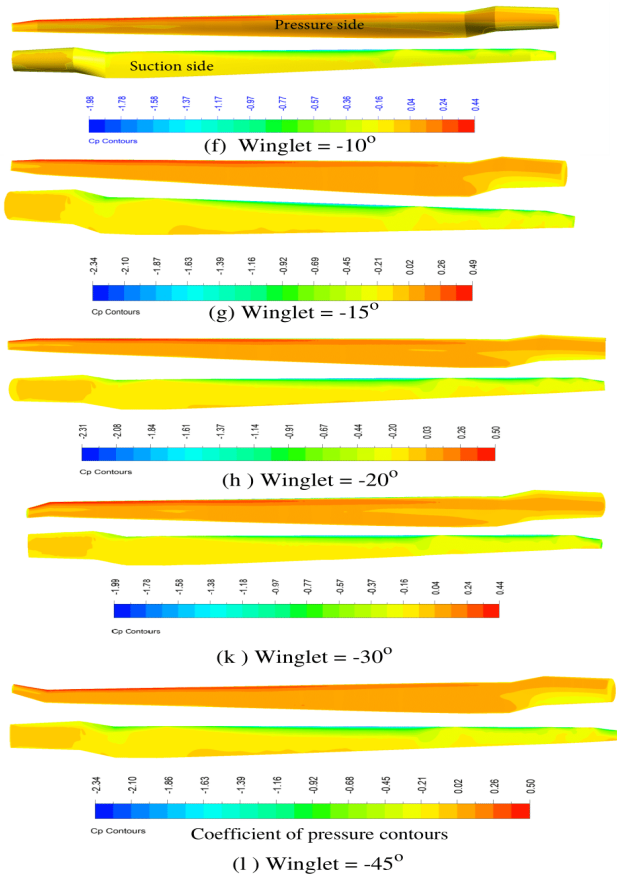
**Figure 12.** Comparison of flap-wise bending load for different winglet configurations

Figure 13 shows pressure coefficient distribution on the baseline blade surfaces.



**Figure 13.** Pressure coefficient distribution on the baseline blade surfaces

The pressure coefficient distribution on the blade surfaces (suction and pressure sides) for all blades with winglets are shown in Figure 14 and 15.



**Figure 14.** Pressure coefficient distribution on the blade surfaces for blades with winglets oriented to the pressure side

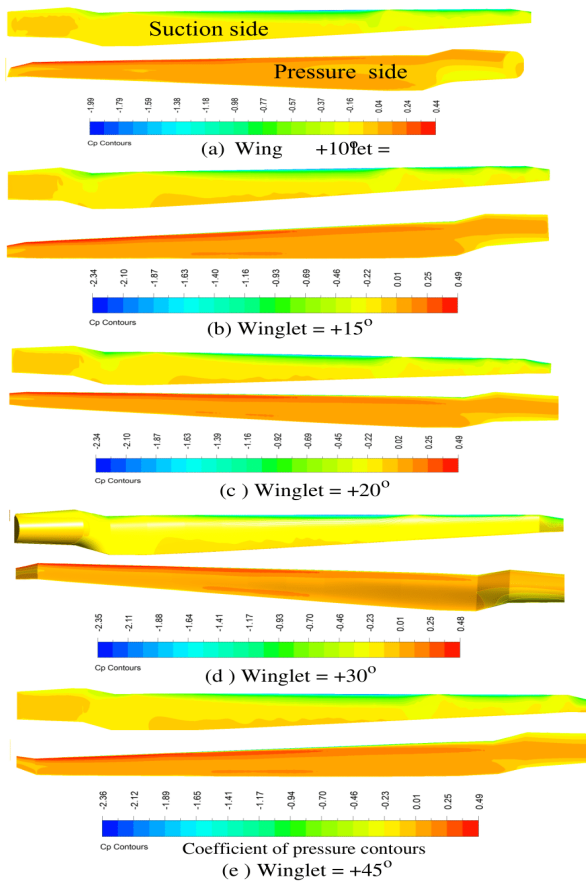


**Figure 15.** Pressure coefficient distribution on the blade surfaces for blades with winglets oriented to the suction side

It has observed that, changing the profile at the blade-tip to incline in either suction or pressure side influences pressure distribution. The highest positive pressure is distributed near the leading edge on the pressure surface, while the highest negative pressure occurred on the same region but on the suction surface as seen in Figures 13, 14 and 15 respectively. What causes the difference in aerodynamic torque and flap-wise bending load, is the variation of pressure difference distributed on the blade surfaces.

Figure 16 illustrates the comparative analysis of changes in aerodynamic torque and flap-wise bending load based on the benchmark blade simulation results.

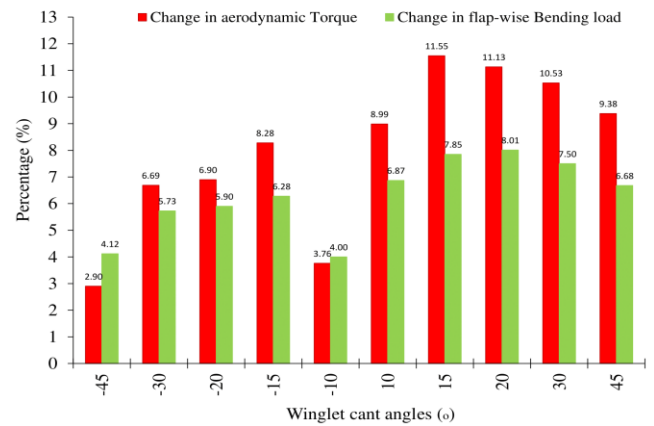


**Figure 16.** Comparison of change in aerodynamic torque and flap-wise bending load with respect to the blade without winglet

By comparing blades B-W7 and B-W8 configurations, the blade designated as B-W7 produces higher aerodynamic torque and lower flap-wise bending load than that of B-W8. The ideal blade was expected to have produced more aerodynamic torque and less flap-wise bending load. The authors argued that massive increase in flap-wise bending load would lead to higher fatigue load, while an increase in aerodynamic torque would decrease the cost of energy. This means that, higher aerodynamic torque would increase wind power output annually, while less flap-wise bending load relieve essential components in the hub from fatigue load, which in turn could either prolong lifespan operation of wind turbine or save on return in investment as a result of low cost in maintenance. Based on this, the best performing blade was selected based on an increase in aerodynamic torque as well as checking the magnitude of flap-wise bending load increased.

The computational analysis presented in Figure 16 shows that orientation and variation of cant angle have significant effects on aerodynamic torque generation and flap-wise bending load. The blades with winglets pointing to the suction side are the most effective as compared to the corresponding blades with winglets pointing to the pressure side. The blade with a winglet tilted at  $-45^\circ$  cant angle, resulted in being the most ineffective design configuration because it increased flap-wise bending load by 4% while sacrificing aerodynamic torque by 2%. The blade with a winglet of  $15^\circ$  produced a maximum increase in aerodynamic torque by 11.5%, and flap-wise bending load by 7.8%. The blade with a winglet of  $20^\circ$  increased aerodynamic torque by 11.1% and flap-wise bending load by 8.0%. Comparing these two blade configurations, slight different margins between

change in aerodynamic torque and flap-wise bending load was found to be 0.4% and 0.2% respectively. Since a less flap-wise bending load is an advantage to wind turbine structure, a small increase in aerodynamic torque is an advantage to energy production and a blade with a winglet of 15° was selected as the best performing configuration in the presented comparative analysis. This blade is designated as B-W7 as presented in Table 2 above.

### 5.3 Effects of a winglet with a change in blade pitch angle

The blade with a winglet (B-W7) was further tested for pitch angle sensitivity. The pitch angle was varied depending on wind speed as shown in Table 3. The wind speed was varied between 11.4 m/s to 25 m/s. The rotational speed of the blade was kept constant at 12.1 rpm in all simulations. CFD simulations were performed, and the obtained aerodynamic torque and flap-wise bending load were compared to simulation results of the straight benchmarked blade. Table 5 presents simulation results on flap-wise bending load and aerodynamic torque computed at different wind speed and pitch angles.

**Table 5.** Comparison of calculated flap-wise bending load and aerodynamic torque

m/s	Pitch angle	Flap-wise bending load (M <sub>Y</sub> )		
		Baseline blade	B-W7	ΔM <sub>Y</sub>
11.4	0.0	9.18	10.28	0.12
13.0	6.6	6.05	6.7	0.092
15.0	10.45	4.45	5.2	0.107
18.0	14.92	3.02	3.7	0.162
20.0	17.47	2.39	3.0	0.429
23.0	21.18	1.69	2.1	0.269
25	23.47	1.27	1.7	0.342
m/s	Pitch angle	Aerodynamic Torque (M <sub>Z</sub> )		
		Baseline blade	B-W7	ΔM <sub>Z</sub>
11.4	0.0	1.44	1.57	0.090
13.0	6.6	1.27	1.38	0.087
15.0	10.45	1.15	1.27	0.108
18.0	14.92	1.07	1.21	0.136
20.0	17.47	1.05	1.23	0.175
23.0	21.18	0.93	1.10	0.190
25	23.47	0.85	1.03	0.210

Computation results displayed in Figure 17 shows comparative of aerodynamic torque plots for blade with and without a winglet with change in pitch angle at different wind speed.

In Figure 17 the difference in margin between aerodynamic torque curves of the blade with a winglet B-W7 and straight baseline blade signifies the resultant effects of adding a winglet. Aerodynamic torque decreased in an almost linear trend when blade pitch angle was increased despite increases in wind speed. A slight abnormality was observed when both blades with and without winglet were pitched by 17.47° at wind speed of 20 m/s. It is not clear to the authors the causes of uncertainties, since all the other operating conditions were kept similar other than the variation in wind speed.

Computational flap-wise bending load for both blade with and without winglet configurations was also examined with a change in blade pitch angle for given wind speeds. Figure 18 shows how flap-wise bending load vary with change in blade pitch angle for both blades with and without winglet

configurations as wind speeds increase.

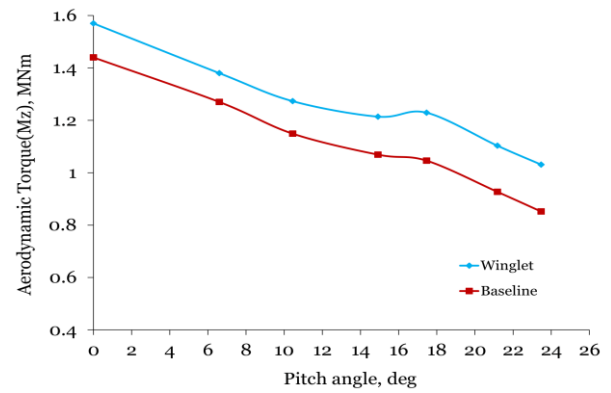


**Figure 17.** Comparison of aerodynamic torque

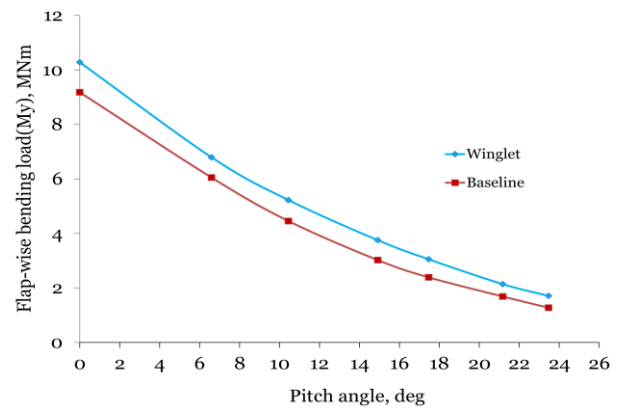


**Figure 18.** Comparison of flap-wise bending load

From Figure 18, it was observed that for both blades with and without the winglet had significant reduction in flap-wise bending load with an increase in pitching angle, despite an increase in wind speed. The gap between the two flap-wise bending load curves signify the margin difference of the obtainable flap-wise bending load between blade with a winglet and the blade without.

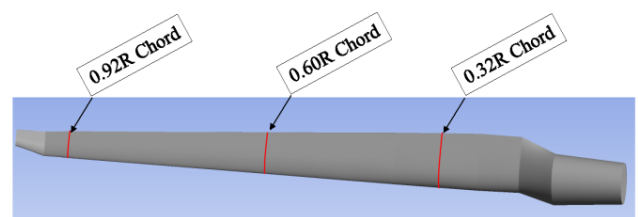
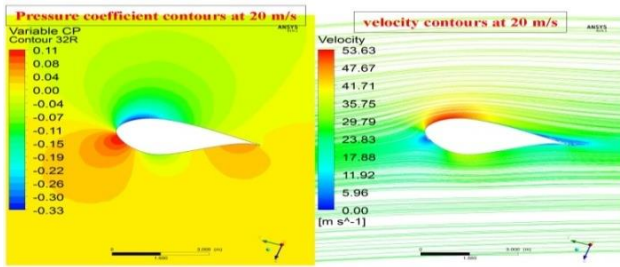
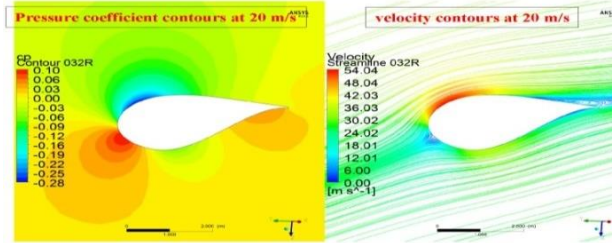


**Figure 19.** Blade with a winglet showing the chords at which pressure coefficient and relative velocity contours were compared for baseline blade at 11.4m/s (0° pitch angle) and 20 m/s (17.47° pitch angle) wind speed

At zero pitch angle, both blade configurations depicted highest aerodynamic torque as well as flap-wise bending load. Aerodynamic torque and flap-wise bending load decrease when the blades were pitched corresponding to its operating conditions. This may be referred to as the pitch-to-feather control scheme, where the sensitivity of aerodynamic torque to the rotor collective blade-pitch angle  $\frac{\partial M_z}{\partial \theta}$  is negative on the region between the rated wind speed and cut-out wind speed (region III) of power curve [16].

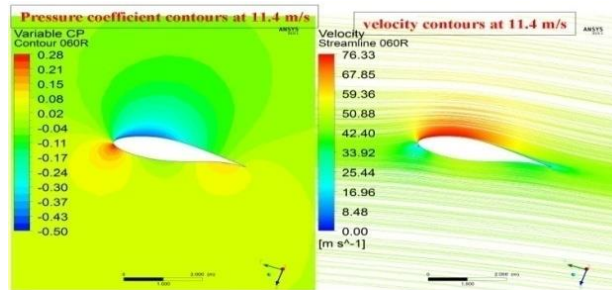


At 0.32R Chord for blade with winglet

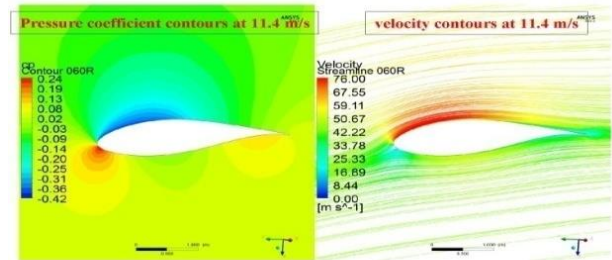


At 0.32R Chord for baseline blade

**Figure 20.** Comparison of pressure coefficient and relative velocity contours of blade with a winglet to that of a straight baseline blade at 0.32R Chord for wind speed of 11.4m/s ( $0^\circ$  pitch angle)



At 0.60R Chord for blade with winglet

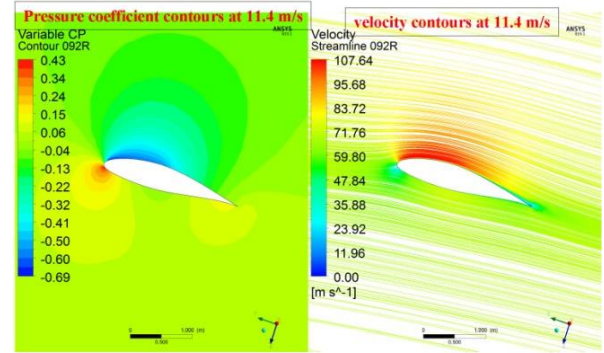


At 0.60R Chord for baseline blade

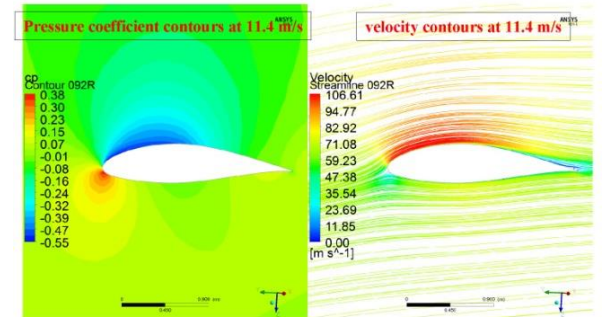
**Figure 21.** Comparison of pressure coefficient and relative velocity contours of blade with a winglet to that of a straight baseline blade at 0.60R Chord for wind speed of 11.4m/s ( $0^\circ$  pitch angle)

From Figures 17 and 18 deduced that both aerodynamic torque and flap-wise bending load depend on pressure distribution over the blade surface. The winglet does not only increase the aerodynamic torque but also increases the flap-wise bending load. The reason could be due to an increase in pressure difference along the blade span due to the employment of winglet which diffuses span-wise free stream towards the blade-tip. This observation is supported by comparisons of pressure coefficient contours and velocity contours at different chord span-wise for a blade with a winglet and the baseline blade. The computations of the pressure coefficient and relative velocity were performed at

wind speeds of 11.4 m/s and 20 m/s for different chords as illustrated in Figure 19.

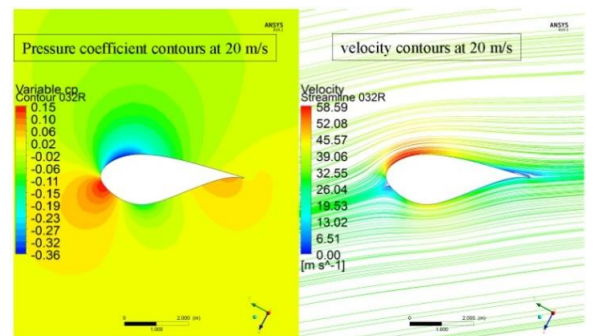


At 0.92R Chord for blade with winglet

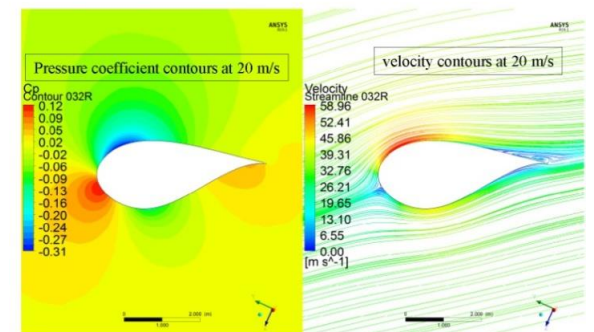


At 0.92R Chord for baseline blade

**Figure 22.** Comparison of pressure coefficient and relative velocity contours of blade with a winglet to that of a straight baseline blade at 0.92R Chord for wind speed of 11.4m/s ( $0^\circ$  pitch angle)

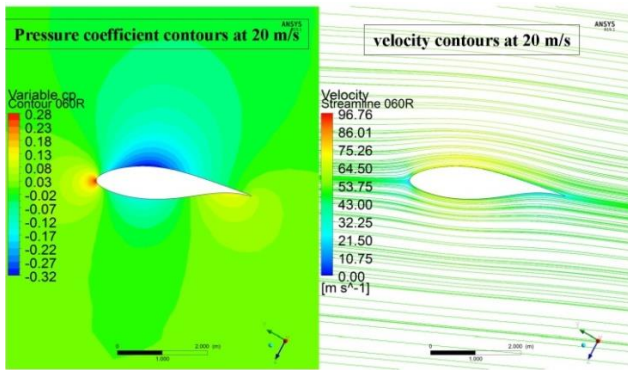


(a) At 0.32R Chord for blade with winglet

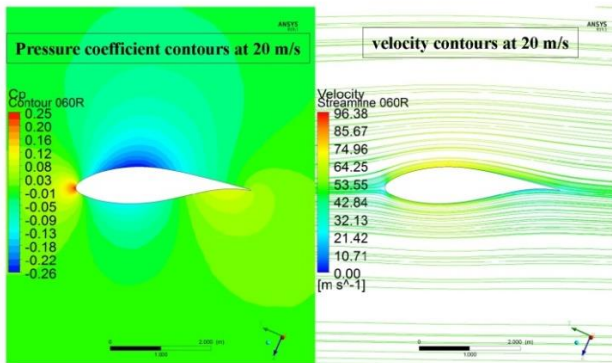


(b) At 0.32R Chord for baseline blade

**Figure 23.** Comparison of pressure coefficient and relative velocity contours of blade with a winglet to that of a straight baseline blade at 0.32R Chord for wind speed of 20 m/s ( $17.47^\circ$  pitch angle)

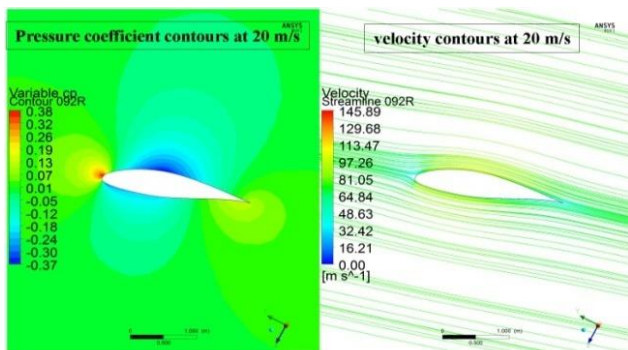


At 0.60R Chord for blade with winglet

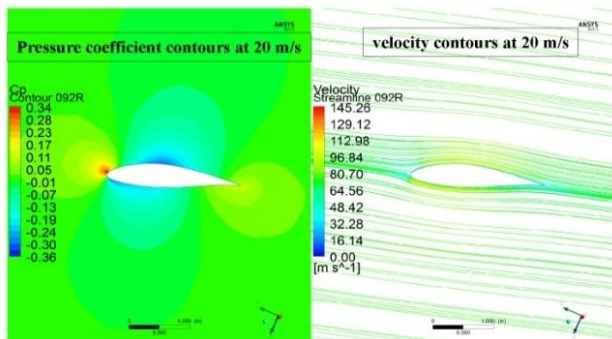


At 0.60R Chord for baseline blade

**Figure 24.** Comparison of pressure coefficient and relative velocity contours of blade with a winglet to that of a straight baseline blade at 0.60R Chord for wind speed of 20 m/s (17.47° pitch angle)



At 0.92R Chord for blade with winglet



At 0.92R Chord for baseline blade

**Figure 25.** Comparison of pressure coefficient and relative velocity contours of blade with a winglet to that of a straight baseline blade at 0.92R Chord for wind speed of 20 m/s (17.47° pitch angle)

Figures 20, 21 and 22 compare pressure coefficient distribution contours and relative velocity contours of a blade with a winglet to that of a baseline blade at 11.4 m/s.

Figures 23, 24 and 25 compare pressure coefficient distribution contours and relative velocity contours of a blade with a winglet to that of the baseline blade at 20 m/s.

According to Imamura et al. [14], an extension of the span by 10% R provided 21% increment of the maximum power output over the baseline rotor blade while a winglet of 10% R height inclined by 80° cant angle increased power output by 22%. Both modifications resulted in almost similar power increment, so an application of winglet can provide an alternative of increasing wind power output without the necessity of increasing the rotor diameter. Application of winglet can therefore be applied where transport and control issues restrict an increase of rotor diameter.

## 6. CONCLUSION

In this study, CFD simulations for blades with blade-tip tilted to the pressure and suction sides have been performed using a single steady moving reference frame. For the first cycle of simulations, the computational results revealed that rotating the blade-tip section to either suction or pressure side have direct effects on increasing the tangential force, axial force, flap-wise bending load and aerodynamic torque. Blades with winglets pointing to the suction side performed better than corresponding blade with winglets pointing to the pressure side both in aerodynamic torque and flap-wise bending load. The blade with a winglet of 15° resulted in the highest increase of aerodynamic torque by 11.5%. The blade with a winglet of 200 produced the highest increase in flap-wise bending load by 8%.

Adjusting the pitch angle affected angle of attack, which in turn influenced the flap-wise bending load and aerodynamic torque. By using pitch-to-feather control scheme, aerodynamic torque and flap-wise bending load decreased with an increase in pitch angle to feather for respective wind speeds. The gaps on the pitch-to-feather curves for aerodynamic torque and flap-wise bending load indicated that the effects of winglet with small angle of inclination (cant angle) equivalent to 15°. It was demonstrated that winglet causes an increase in aerodynamic torque with a slight increase in flap-wise bending load.

## 7. FUTURE WORK

The further work afore looks for more CFD simulations of the selected blade B-W7 at wind speed below rated wind speeds. Transient simulations using sliding mesh will also be performed, and the results compared to those from a steady single rotating frame in order to account for most accurate CFD method. Another aspect to be investigated is the aerodynamic effect of winglet curvature connecting with the main blade profile.

## ACKNOWLEDGEMENTS

The authors acknowledge support from Mobility to Enhance Training of Engineering Graduates in Africa (METEGA) under the Intra ACP Mobility Schemes. We also

wish to acknowledge Dr Joshua K Ngoret for proof reading this paper.

## REFERENCES

- [1] Granovskii, M., Dincer, I., Rosen, M.A. (2007). Greenhouse gas emissions reduction by use of wind and solar energies for hydrogen and electricity production: Economic factors. *International Journal of Hydrogen Energy*, 32(8): 927-931. <https://doi.org/10.1016/j.ijhydene.2006.09.029>
- [2] Wisler, R., Hand, M., Seel, J., Paulos, B. (2016). Reducing wind energy costs through increased turbine size: Is the sky the limit. *Rev. Berkeley National Laboratory Electricity Markets and Policy Group*.
- [3] Gielen, D., (2012). Renewable energy technologies: cost analysis series. *Sol Photovolt*. 1(4-5): 52.
- [4] Chu, S., Majumdar, A. (2012). Opportunities and challenges for a sustainable energy future. *Nature*, 488(7411): 294-303. <https://doi.org/10.1038/nature11475>
- [5] Tjiu, W., Marnoto, T., Mat, S., Ruslan, M.H., Sopian, K. (2015). Darrieus vertical axis wind turbine for power generation II: Challenges in HAWT and the opportunity of multi-megawatt Darrieus VAWT development. *Renewable Energy*, 75: 560-571. <https://doi.org/10.1016/j.renene.2014.10.039>
- [6] Johansen, J., Sørensen, N.N. (2007). Numerical analysis of winglets on wind turbine blades using CFD. *Proceedings of the European Wind Energy Congress*. Citeseer.
- [7] Jones, R.T., Lasinski, T.A. (1980). Effect of winglets on the induced drag of ideal wing shapes. *NASA Technical Memorandum*, 81230(81): 70009.
- [8] Maughmer, M.D. (2003). Design of winglets for high-performance sailplanes. *Journal of Aircraft*, 40(6): 1099-1106. <https://doi.org/10.2514/2.7220>
- [9] Smith, M., Komerath, N., Ames, R., Wong, O., Pearson, J. (2001). Performance analysis of a wing with multiple winglets. In *19th AIAA Applied Aerodynamics Conference*. <https://doi.org/10.2514/6.2001-2407>
- [10] Gaunaa, M., Johansen, J. (2007). Determination of the maximum aerodynamic efficiency of wind turbine rotors with winglets. In *Journal of Physics: Conference Series*. IOP Publishing. <https://doi.org/10.1088/1742-6596/75/1/012006>
- [11] Gupta, A., Amamo, R. (2012). CFD analysis of wind turbine blade with winglets. in *ASME 2012 International Design Engineering Technical Conferences and Computers and Information in Engineering Conference*. American Society of Mechanical Engineers Digital Collection, <https://doi.org/10.1115/DETC2012-70679>
- [12] Godsk, K.B., Nielsen, T.S.B. (2011). Wind turbine with rotor blades equipped with winglets and blades for such rotor. <https://patents.google.com/patent/US7931444B2/en>.
- [13] Elfarrar, M.A., Sezer Uzol, N., Akmandor, İ.S. (2015). Investigations on blade tip tilting for HAWT rotor blades using CFD. *International Journal of Green Energy*, 12(2): 125-138. <https://doi.org/10.1080/15435075.2014.889007>
- [14] Imamura, H., Hasegawa, Y., Kikuyama, K. (1998). Numerical analysis of the horizontal axis wind turbine with winglets. *JSME International Journal Series B Fluids and Thermal Engineering*, 41(1): 170-176. <https://doi.org/10.1299/jsmeb.41.170>
- [15] Lawton, S., Crawford, C. (2014). Investigation and optimization of blade tip winglets using an implicit free wake vortex method. In *Journal of Physics: Conference Series*. IOP Publishing. <https://doi.org/10.1088/1742-6596/524/1/012033>
- [16] Jonkman, J., Butterfield, S., Musial, W., Scott, G. (2009). Definition of a 5-MW reference wind turbine for offshore system development. *National Renewable Energy Lab. (NREL)*, Golden, CO, United States. <https://doi.org/10.2172/947422>
- [17] Mourits, G. (2014). BEM theory and CFD for wind turbine aerodynamics. *Internship Report*, University of Twente & University of Liverpool.
- [18] Ariff, M., Salim, S.M., Cheah, S.C. (2009). Wall y+ approach for dealing with turbulent flow over a surface mounted cube: Part 1-Low Reynolds Number. in *Seventh International Conference on CFD in the Minerals and Process Industries*, CSIRO, Melbourne, Australia.
- [19] Muiruri, P.I., Motsamai, O.S., Ndeda, R. (2019). A comparative study of RANS-based turbulence models for an upscale wind turbine blade. *SN Applied Sciences*, 1(3): 237. <https://doi.org/10.1007/s42452-019-0254-5>
- [20] Fluent, A. (2017). *ANSYS Fluent Theory Guide*, Release 18.0. Ansys. Inc
- [21] Bazilevs, Y., Hsu, M.C., Akkerman, I., Wright, S., Takizawa, K., Henicke, B., Spielman, T., Tezduyar, T. (2011). 3D simulation of wind turbine rotors at full scale. Part I: Geometry modeling and aerodynamics. *International Journal for Numerical Methods in Fluids*, 65(1-3): 207-235. <https://doi.org/10.1002/flid.2400>
- [22] Siddiqui, M.S., Rasheed, A., Kvamsdal, T., Tabib, M. (2017). Quasi-Static & Dynamic Numerical Modeling of Full Scale NREL 5MW Wind Turbine. *Energy Procedia*. 137: 460-467. <https://doi.org/10.1016/j.egypro.2017.10.370>
- [23] Siddiqui, M.S., Rasheed, A., Tabib, M., Kvamsdal, T. (2016). Numerical analysis of NREL 5MW wind turbine: A study towards a better understanding of wake characteristic and torque generation mechanism. in *Journal of Physics: Conference Series*. IOP Publishing, <https://doi.org/10.1088/1742-6596/753/3/032059>
- [24] Zhao, W.C., Cheng, P., Wan, D.C. (2014). Numerical computation of aerodynamic performances of NREL offshore 5-MW baseline wind turbine. *The Eleventh ISOPE Pacific/Asia Offshore Mechanics Symposium*, Shanghai, China.